 DOI 10.1002/mawe.202000287

Influence of contour scans on surface roughness and pore formation using Scalmalloy® manufactured by laser powder bed fusion (PBF-LB)

Einfluss der Konturbelichtung auf die Oberflächenrauheit und Porenbildung von Scalmalloy® beim pulverbettbasierten Schmelzen mittels Laserstrahl

T. Reiber[1], J. Rüdesheim[1], M. Weigold[1], E. Abele[1], J. Musekamp[2], M. Oechsner[2]

The scandium modified aluminium alloy Scalmalloy® is specifically developed for the use in laser-based powder bed fusion (PBF-LB). It is supposed to show potential in the production of lightweight structures due to its high specific strength compared to other aluminium alloys. A limiting factor is the high surface roughness of additively manufactured parts, which has a negative influence on its mechanical properties, especially under cyclic loads. In order to reduce the surface roughness, methods of design of experiments (DoE) are applied to develop contour parameters. Additionally, the formation of pores in keyhole-mode welding and strategies to reduce the porosity in the contour area are investigated. The surface roughness of vertical walls can be reduced down to $Ra < 7$ µm using contour scans with a line energy $E_L > 0.9\,\mathrm{J\,mm^{-1}}$ but keyhole pores start to form applying $E_L > 0.6$–$0.75\,\mathrm{J\,mm^{-1}}$. Two contour parameter sets in different E_L-ranges are developed that can be used to reduce the surface roughness compared to parameter sets without contour scans, without increasing the porosity in the contour area. Their impact on the mechanical properties has to be further investigated.

Keywords: Additive manufacturing **/** Surface roughness **/** Keyhole-mode welding **/** Melt pool dimensions **/** Contour porosity

Die scandiumhaltige Aluminiumlegierung Scalmalloy® ist speziell für die Verwendung beim pulverbettbasierten Schmelzen mittels Laserstrahl entwickelt worden. Durch die im Vergleich zu anderen Aluminiumlegierungen hohe spezifische Festigkeit birgt sie ein besonders Potenzial in der Fertigung von Leichtbaubaustrukturen. Ein begrenzender Faktor ist dabei die hohe Oberflächenrauheit additiv gefertigter Bauteile, die einen negativen Einfluss auf die mechanischen Festigkeitseigenschaften insbesondere unter zyklischer Belastung ausübt. Um die Oberflächenrauheit zu reduzieren werden mit Methoden der statistischen Ver-

[1] Technical University of Darmstadt, Institute of Production Management, Technology and Machine Tools (PTW), Otto-Berndt-Straße 2, 64287 DARMSTADT, GERMANY

[2] Technical University of Darmstadt, Center for Engineering Materials, State Materials Testing Institute Darmstadt (MPA) Chair and Institute for Materials Technology (IfW), Grafenstraße 2, 64283 DARMSTADT, GERMANY

Corresponding author: T. Reiber, Technical University of Darmstadt, Institute of Production Management, Technology and Machine Tools (PTW), Otto-Berndt-Straße 2, 64287 DARMSTADT, GERMANY,
E-Mail: t.reiber@ptw.tu-darmstadt.de

suchsplanung Konturparameter entwickelt. Zusätzlich werden die Bildung von Keyhole-Poren und Strategien zur Reduzierung der oberflächennahen Porosität untersucht. Dabei kann gezeigt werden, dass die Oberflächenrauheit vertikaler Oberflächen auf eine Rauheit von $Ra < 7$ µm durch eine Konturbelichtung mit $E_L > 0.9\ \mathrm{J\,mm^{-1}}$ reduziert werden kann. Ab $E_L > 0.6$–$0.75\ \mathrm{J\,mm^{-1}}$ tritt jedoch die Bildung von Keyhole-Poren ein. Es können zwei Konturparametersätze in verschiedenen E_L-Bereichen identifiziert werden, mit denen eine Reduktion der Oberflächenrauheit im Vergleich zu Parametersätzen ohne Konturparameter ermöglicht wird, ohne dabei die Porosität in der Konturregion zu erhöhen. Den Einfluss der Konturbelichtung auf die mechanischen Eigenschaften gilt es weiter zu untersuchen.

Schlüsselwörter: Additive Fertigung / Oberflächenrauheit / Tiefschweißen / Schmelzbaddimensionen / oberflächennahe Porosität

1 Introduction

In laser-based powder bed fusion (PBF-LB), powder material is melted layer by layer by a laser, allowing components with high performance and functionality to be produced while saving raw materials, costs and energy [1]. This can be achieved by utilizing the high degree of design freedom, but also by using newly developed materials for this process. Scalmalloy® is an aluminium-magnesium-scandium alloy developed by APWorks GmbH which allows to achieve up to 70 % higher tensile and fatigue strength compared to other aluminium alloys [2]. The addition of scandium and magnesium as alloying elements ensures small grain sizes and thus high ductility, but also allows the material to be hardened by the precipitation of Al_3Sc and MgO [3, 4]. In parallel to the microstructure and mechanical properties such as strength and hardness, the achievable component density has been investigated, where densities of up to 99.98 % were attained [2, 5–8].

During contour scans, material is melted in one or more vectors parallel to the contour of the component. The contour can be exposed before the infill (pre-contour) or after the infill (post-contour). In µSLM a lower roughness can be achieved when using pre-contours, as these can serve as a barrier for the melt pools of the infill [9]. However, these might increase the elevation of edges and the thinning of the powder bed along the scan track causing connection defects [10]. The process parameters of the contour scans can be optimized independently of the infill parameters with regard to a low surface roughness. Increased energy input can lead to a lower surface roughness, as more uniform melt tracks are created and the peaks and valleys between layers can be reduced by re-melting them [11]. A parameter to determine the energy input is the line energy E_L, which is given by the ratio of the laser power P and scanning speed v. Partly, a roughness of $Ra = 6.1$ µm was achieved on Scalmalloy® specimens when applying two contour scans with a high line energy $E_L = 1.17\ \mathrm{J\,mm^{-1}}$, but pores were apparent along the contour scans [8]. As pores, especially close to the surface, and high surface roughness have a negative effect on mechanical properties such as fatigue strength, both have to be avoided [11, 12].

The reason for the occurrence of pores when exposing with high line energies can be the transition from conduction-mode to keyhole-mode welding. In conduction-mode welding, the shape of the melt pool is defined by the thermal conductivity of the surrounding material. From a transition temperature onwards, the recoil pressure of evaporating material thrusts parts of the melt pool aside so the laser beam can penetrate deeper into the material, thereby creating a keyhole [13]. Since the recoil pressure is greatest at the bottom of the keyhole, the melt is displaced to the rear. As the laser continues moving forward, the melt pool flows down from areas of lower recoil pressure and higher surface tension and traps gas bubbles within the melt pool, creating keyhole pores [14], *Figure 1*. With deeper keyholes this effect is enhanced due to an increasing difference in recoil pressure and surface tension between the top surface and the bottom of the keyhole [14].

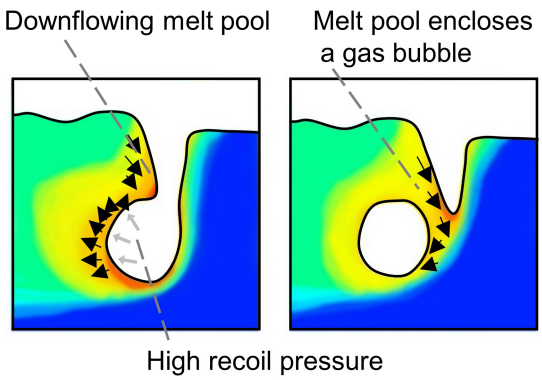

Figure 1. Formation of keyhole pores after [14].

To classify the different welding modes, the aspect ratio A_N of the melt pool depth d_d to width d_w can be used. With $A_N = 0.5$, the melt pool expands uniformly in all directions. When transitioning to keyhole-mode welding the depth of the melt pool increases disproportionally causing the aspect ratio to increase above 0.5. Different threshold values are used in the literature, ranging from 0.5 to 2, sometimes adding a third transition welding mode in between conduction and keyhole-mode welding [6, 13, 15, 16]. The present welding mode is influenced by the material properties and the process parameters and can be set via laser power, scanning speed and focus diameter [13]. The laser power has a more significant influence on the welding mode than the scanning speed, using calorimetric measurements to determine the degree of energy absorption which is linked to the welding mode [17].

To prevent the formation of keyhole pores, keyhole-mode welding can be avoided by reducing the line energy. Another concept for the reduction of pores is the re-melting of the solidified material whereby a reduction of the amount of gas pores in infill and upskin areas has been achieved [18–20].

The aim of this study is to reduce the surface roughness of vertical surfaces of specimens built out of Scalmalloy® by using contour scans, without generating additional pores in the contour area. For this purpose, the parameter-dependent melt pool dimensions are initially determined in preliminary tests. Using methods of design of experiments (DoE) different contour scanning strategies are investigated in two parameter fields with different line energy (E_L)-ranges. Finally, based on the results, the investigated parameter field is extended to further improve the achievable part properties.

2 Methods

2.1 Laser powder bed fusion system and metal-powder material

The experiments are conducted on a laser-based powder bed fusion system EOS M 290. The Yb-fiber laser utilized has a recommended maximum laser power of 370 W and a focus diameter of 100 µm. Using a F-theta lens the laser is aligned perpendicular to the building platform over a wide range, which has a proven effect on surface roughness [21]. The maximum building volume is 250 mm × 250 mm × 325 mm. During the build process, the build chamber is inerted with argon to keep the oxygen content below 0.1 %. For the exposure of the infill, a valid parameter set is applied in all experiments, which allows to achieve a component density > 99.8 % and a surface roughness of $Ra = 15$ µm at a layer height of 0.03 mm, *Table 1*. The Scalmalloy® powder from Heraeus Additive Manufacturing GmbH has been recycled from previous builds by sieving out coarse particles, *Table 2*.

2.2 Experimental design

To determine the melt pool dimensions, single track experiments are carried out in a wide E_L-range between 0.08 J mm^{-1} and 1.85 J mm^{-1}. These are used to determine the parameter-dependent melt

Table 1. Infill parameter set for Scalmalloy®, utilizing time homogenization. The strategy time homogenization is a feature developed by EOS GmbH and included in the software EOSPRINT 2 [22].

Laser power, P [W]	370
Scan speed, v [mm s^{-1}]	1600
Hatch distance, h [mm]	0.07
Exposure pattern	Stripes
Stripe width [mm]	7
Layer rotation	67°

Table 2. Chemical composition of the Scalmalloy® powder specified by the manufacturer. Particle size distribution of the used powder: $d_{10} = 20$ µm, $d_{50} = 39$ µm, $d_{90} = 61$ µm (rounded to whole numbers).

Element	Concentration [mass-%]
Al	Balance
Mg	< 7
Sc	< 2
Zr	< 1
Mn	< 1

pool width to calculate the percentage overlap o_{ci} of the contour scan with the infill. Furthermore, the aspect ratio of the melt pool depth to melt pool width A_N can be utilized to determine the weld mode. For this purpose, 10 mm long melt tracks (12 per parameter set) are built on top of 23 mm high cuboids, which are produced in the same build job, *Figure 2*. To ensure that the melt tracks are easily distinguishable from the melt tracks of the layer below, the scan vectors of the last regular layer are rotated by 90° to the melt tracks being examined.

To investigate the influence of the contour parameters and the contour scanning strategy on the surface roughness and contour porosity, cuboid specimens are produced and analysed using methods of design of experiments (DoE). In order to map non-linear relationships a face-centred central composite design (FCCD) is chosen with three factor levels and a six-fold production of the centre point. Based on the results, regression models are created and an analysis of variance (ANOVA) is performed to identify significant effects. To validate the models, additional specimens are produced, that are not included in the creation of the model. On that basis, the predicted and actual values can be compared.

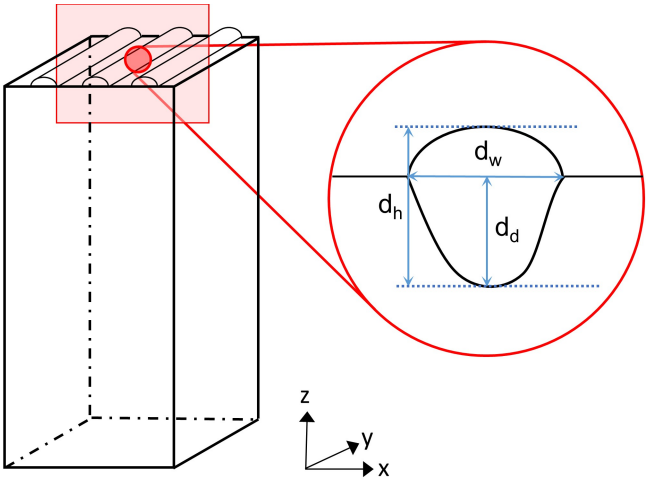

Figure 2. Specimen with single melt tracks on top of a cuboid (proportions not true to scale) with a section of a melt pool orthogonal to the exposure direction of the melt track illustrating the maximum melt pool width d_w, depth d_d and the total height d_h.

Within the scope of preliminary tests, two concepts are investigated: the exposure of a pre-contour in a low E_L-range and the exposure of two post-contours in a high E_L-range. The division into two E_L-ranges allows a better representation of the pore formation associated with the transition to keyhole-mode welding at high line energies. In the low E_L-range, there is no keyhole pore formation to be expected. A pre-contour is chosen since preliminary tests at low line energies show lower surface roughness with pre- compared to post-contours ($E_L = 0.14\ \mathrm{J\,mm^{-1}}$, pre-contour: $Ra = 14.6$ µm, post-contour: $Ra = 26.9$ µm). The three process parameters investigated are laser power P, scan speed v and the percentage overlap o_{ci} of the contour with the infill, *Table 3*, *Figure 3*. The combinations of P and v result in an E_L-range from $0.14\ \mathrm{J\,mm^{-1}}$ to $0.62\ \mathrm{J\,mm^{-1}}$. Parameters with $o_{ci} < 50$ % are not investigated to guarantee sufficient connection between the contour scan and the infill.

In the second parameter field at a high E_L-range a lower surface roughness but also increased pore formation are expected, as observed in preliminary tests. Through the exposure of a second post-contour, re-melting parts of the previous contour scan, it is intended to reduce the amount of pores introduced by the first post-contour. By re-melting

Table 3. Contour parameter factor levels of the DoE for the experiments in the low E_L-range.

Factors		Levels		
		−1	0	+1
P	[W]	230	300	370
v	[mm s^{-1}]	600	1100	1600
o_{ci}	[%]	50	70	90

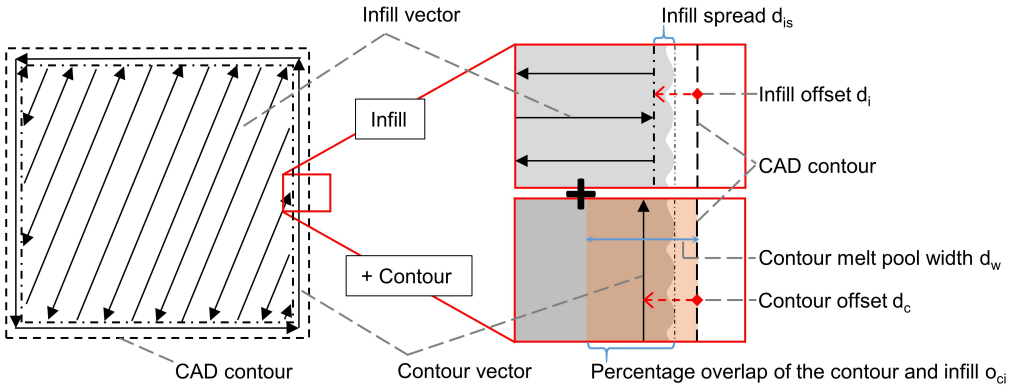

Figure 3. Contour and infill vectors and their offsets to the CAD contour. Additionally, the percentage overlap of the contour scan and the infill o_{ci} depending on the contour melt pool width d_w, infill offset d_i, infill spread d_{is} and contour offset d_c is illustrated.

the contour area, entrapped gas bubbles can potentially rise to the surface eliminating the pore. Therefore, the line energy of the second post-contour must be high enough so that the melt pool is deep enough to reach the pores. At the same time, the line energy must be lower than the conditions for the formation of keyhole pores. In this experiment, the laser power of the second post-contour is reduced compared to the laser power of the first post-contour. As a result, the scanning speed is lower for the same line energy, so that the melt pool stays intact longer and favourable conditions for the gas bubbles to rise should be given. The second post-contour is slightly shifted towards the inside of the component (percentage overlap of the second with the first post-contour $o_{cc} > 100\ \%$) to prevent the surface roughness from rising due to the second post-contour while still re-melting the relevant areas of the first post-contour. The three process parameters investigated are E_{L1}, E_{L2} and o_{cc}, *Table 4*.

The percentage overlap of the contour scan with the infill can be set by the infill and contour offsets, Figure 3. By setting the offsets, the final dimensions of the melt pools, like the spread of the infill melt pools towards the CAD contour d_{is} and the width of the contour melt pool d_w, have to be considered. The infill offset d_i marks the distance from the CAD contour to the beginning/end of the infill vectors, Figure 3, top right. The contour offset is the distance from the CAD contour to the parallel contour scan vectors, Figure 3, bottom right. By setting the contour offset to half the contour melt pool width, the final part contour matches the CAD contour. The percentage overlap o_{ci} of the contour scan with the infill is set by adjusting the infill offset d_i, using *Formula 1*. When using two post-contours the percentage overlap of the two contours o_{cc} is set adjusting the contour offset of the inner post-contour d_{ci}.

Table 4. Contour parameter factor levels of the DoE for the experiments in the high E_L-range. The laser power is set to 370 W in the first and 230 W in the second post-contour. The overlap of the first contour with the infill is kept constant at $o_{ci} = 50$ %.

Factors		Levels		
		−1	0	+1
E_{L1}	[J mm^{-1}]	0.6	0.75	0.9
E_{L2}	[J mm^{-1}]	0.55	0.75	0.95
o_{cc}	[%]	100	120	140

$$d_i = 0.5\ d_w + d_c + d_{is} - o_{ci} \cdot d_w \quad (1)$$

2.3 Measurement design

To determine the dimensions of the melt pools, the cuboids are ground and polished with the cross section transverse to the direction of exposure of the melt pools. The surface is subsequently etched with a solution containing hydrofluoric acid and hydrogen peroxide at room temperature to make the boundaries of the individual melt tracks become visible. Using a

digital microscope Keyence VHX-5000 the maximum width d_w, the depth d_d and the total height d_h are measured for each melt track, Figure 3. For the calculation of the aspect ratio A_N, which is used to specify the welding mode, the depth d_d is used instead of the height d_h. This is to avoid the influence of balling effects, which cause the height to increase but not the depth of the weld pool [23]. From $A_N > 0.5$ this work refers to keyhole-mode welding, as from this point the melt pool spreads out further downwards than sideways. A subdivision into a transition area is not carried out.

To quantify the surface roughness, the roughness parameters *Ra* and *Rz* are determined using a tactile measurement system MahrSurf GD25. Following the guidelines of [24] for surfaces with an expected $Ra < 10$ µm a total measuring distance of 17.5 mm and a cut-off filter of 2.5 mm is used. The roughness is measured along five tracks on the specimen side facing the coater, *Figure 4*.

To measure the contour porosity Φ_C, micrographs of the specimens are evaluated in the x-y plane, Figure 4. Therefor the specimens are embedded in epoxy resin and ground down to the examination plane. The specimens are then polished to a grain size of 1 µm. Images of the polished surfaces are taken with a Zeiss Smartzoom5 digital microscope at 100x magnification and a resolution of 2.23 µm per pixel. These are evaluated using a Matlab® script, in which a stripe of 850 µm along the contour is defined as the contour area, Figure 4.

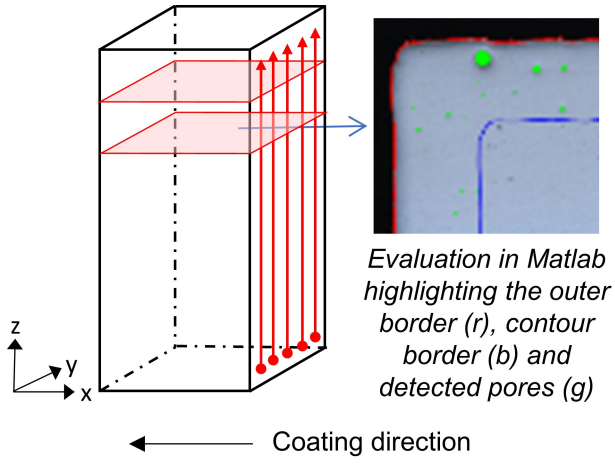

Figure 4. Measuring sections of the cuboid specimens in the x-y plane (left) and part of a micrograph with the marked locations outer border (*red*), contour border (*blue*) and the detected pores (*green*) using Matlab® (right).

Within this area, all pores are assigned to the contour. The contour porosity is determined by evaluating two micrographs per specimen with Φ_C being defined as the quotient of the area of the pores in the contour area and the contour area of the specimen.

3 Results

In this section, the results of the parameter-dependent melt pool dimensions melt pool width d_w, which is required for the calculation of the percentage overlap of the melt pools, and aspect ratio A_N, for the classification of the welding modes, are presented. Moreover, the influence of the selected factor level combinations on the target values surface roughness *Ra* and contour porosity Φ_C within the two E_L-ranges is presented with the help of the determined regression models.

3.1 Melt pool dimensions

The melt pool width develops similar for all laser power levels starting from $P = 230$ W, *Figure 5*. Up to $E_L = 0.5\ \mathrm{J\,mm^{-1}}$, the melt pool width increases with rising E_L and then the curves flatten slightly to a constant gradient. A small dependence of the melt pool width on the laser power is recognizable, whereby the melt pool is wider at a higher laser power but same line energy. At $P = 160$ W and 195 W, the melt pool width increases much slower with a higher variation of the individual measurement results. To calculate the melt pool width depending on the line energy, second-degree polynomials are fitted to the measuring points, *Table 5*.

The results of A_N show a more distinct difference between the different power levels compared

Table 5. Polynomials for different laser powers *P* used to calculate the melt pool width d_w.

P	Polynomial	R^2
230 W	$d_w = -133.16\ E_L^2 + 421.91\ E_L + 72.76$	0.9908
300 W	$d_w = -132.62\ E_L^2 + 452.69\ E_L + 83.82$	0.9825
370 W	$d_w = -95.259\ E_L^2 + 401.19\ E_L + 99.09$	0.9897

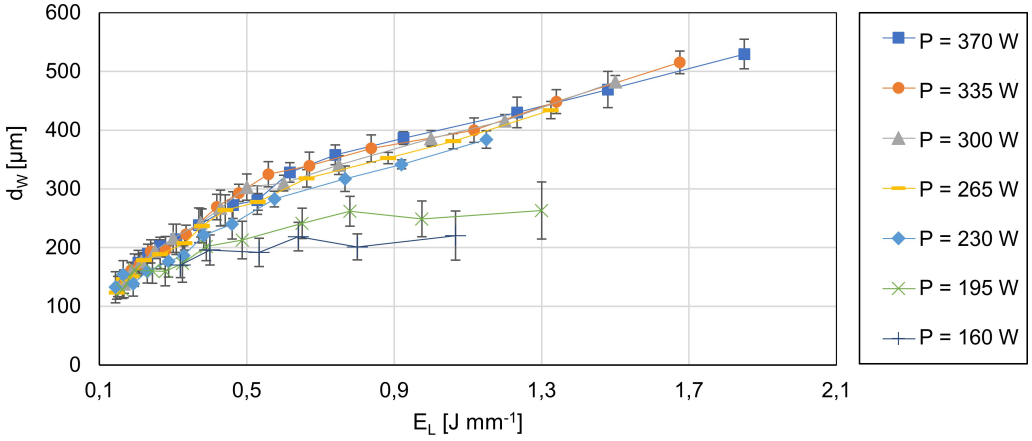

Figure 5. Melt pool width d_w dependent on the line energy E_L and laser power P.

to the results of d_w. For $E_L < 0.5\ \mathrm{J\,mm^{-1}}$ A_N is in the same range for all power levels $P \geq 230$ W, *Figure 6*. With the transition to keyhole-mode welding at $A_N = 0.5$, which is reached at around $E_L = 0.5\ \mathrm{J\,mm^{-1}}$, A_N rises more steeply. This can be explained with the formation of the keyhole causing the melt pool to disproportionately become deeper. For each laser power level a plateau is reached where A_N does not further increase, meaning d_w and d_d increase evenly. At 230 W this plateau is reached from $E_L = 0.77\ \mathrm{J\,mm^{-1}}$ with $A_N = 0.65$, at 370 W A_N increases to about 1.16 from $E_L = 1.23\ \mathrm{J\,mm^{-1}}$. At $P = 160$ W and 195 W A_N remains mostly constant. Micrographs show that at this laser power, the substrate layer is barely melted and the shape of the melt track is influenced by balling, *Figure 7*A_1, A_2.

With the transition from conduction mode welding starting at $A_N = 0.5$, the top view also shows how the shape of the melt pool surface is more distinctly determined by the melt fronts displaced backwards by the recoil pressure than by the surface tension of the melt, Figure 7B_2. Larger keyhole pores occur from $E_L > 0.75\ \mathrm{J\,m^{-1}}$, where $A_N = 0.67$–0.82, Figure 7C_1.

3.2 Regression model – low E_L-range

The results of the experiments are used to create regression models and perform an ANOVA. Since the evaluation shows that P and v alone do not have a significant influence on the surface roughness, E_L is used as a parameter instead. In the evaluation of the regression models, only *Ra* is discussed, but

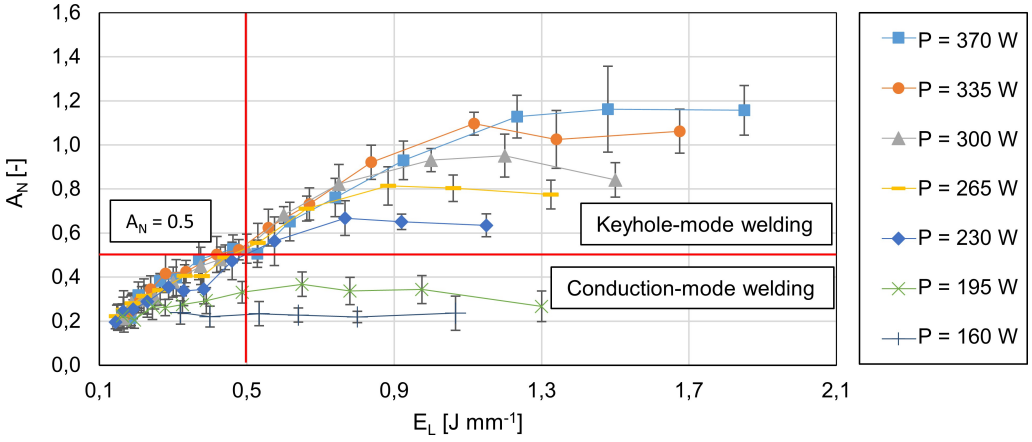

Figure 6. Aspect ratio A_N of the melt pool depth d_d to width d_w dependent on the line energy E_L and laser power P.

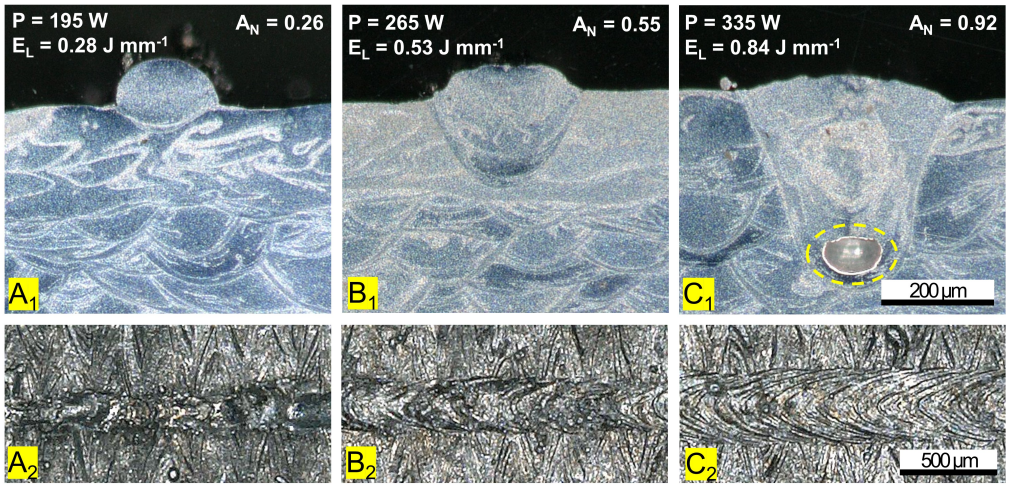

Figure 7. Micrographs and top views from melt pools at different line energies E_L and aspect ratios A_N. A keyhole pore formed at the bottom of the melt pool with $E_L = 0.84\ \mathrm{J\,mm^{-1}}$ (C_1).

Table 6. Key figures for the regression model and the ANOVA of the DoE at low E_L-range used to map the surface roughness *Ra*. A p-value lower than the significance threshold of 0.05 indicates a significant effect on the response variable. The coded coefficient describes the size and direction of the relationship between the term and the response variable.

Ra	Model	Considered terms		
		E_L	o_{ci}	E_L * o_{ci}
p-value	0.000	0.016	0.000	0.000
Coeff.		2.181	2.976	4.291

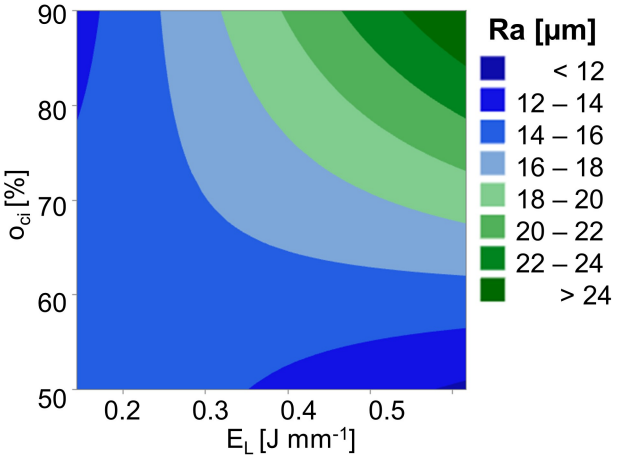

Figure 8. Contour plot in the low E_L-range of surface roughness *Ra* vs line energy E_L and percentage overlap of the contour scan with the infill o_{ci}.

there are no notable differences to the development of *Rz*. Both E_L and o_{ci} are significant terms in the regression model, *Table 6*. The lowest surface roughness $Ra = 11.6\ \mu\mathrm{m}$ is achieved with the highest $E_L = 0.62\ \mathrm{J\,mm^{-1}}$, *Figure 8*. A further local minimum with $Ra = 13.2\ \mu\mathrm{m}$ is attained applying the lowest $E_L = 0.14\ \mathrm{J\,mm^{-1}}$. The influence of o_{ci} on the surface roughness is smaller at a low E_L, whereas at higher E_L the roughness rises significantly as o_{ci} increases, Figure 8.

As there is no observable keyhole pore formation in this E_L-range that would cause Φ_C to rise, only selected micrographs are considered in the discussion.

3.3 Regression model – high E_L-range

In the high E_L-range applying two post-contours the surface roughness is predominantly influenced by E_{L1}, decreasing with increasing E_{L1}, *Table 7*, *Figure 9*. E_{L2} and o_{cc} have no significant influence on the surface roughness, although it increases slightly with increasing E_{L2} and decreasing o_{cc}. The lowest roughness of $Ra = 6.1\ \mu\mathrm{m}$ is achieved with high $E_{L1} = 0.9\ \mathrm{J\,mm^{-1}}$, low $E_{L2} = 0.55\ \mathrm{J\,mm^{-1}}$ and high $o_{cc} = 140\ \%$, Figure 9. However, the porosity with these parameters is very high at $\Phi_C = 0.8\ \%$, *Figure 10*. The lowest porosity of $\Phi_C = 0.16\ \%$ can be achieved at low $E_{L1} = 0.63\ \mathrm{J\,mm^{-1}}$, low $E_{L2} = 0.55\ \mathrm{J\,mm^{-1}}$ and low $o_{cc} = 100\ \%$ ($Ra = 10.2\ \mu\mathrm{m}$). All three basic parameters have a

Table 7. Key figures for the regression model and the ANOVA of the DoE in the high E_L-range used to map the surface roughness *Ra* and contour porosity Φ_C. Basic terms are included in the regression model even if there is no statistically significant association.

Ra	Model	Considered terms		
		E_{L1}	E_{L2}	o_{cc}
p-value	0.000	0.000	0.173	0.688
Coeff.		−2.105	0.459	−0.132

Φ_C	Model	Considered terms			
		E_{L1}	E_{L2}	o_{cc}	E_{L1}^2
p-value	0.000	0.000	0.028	0.029	0.042
Coeff.		0.484	0.208	0.206	0.267

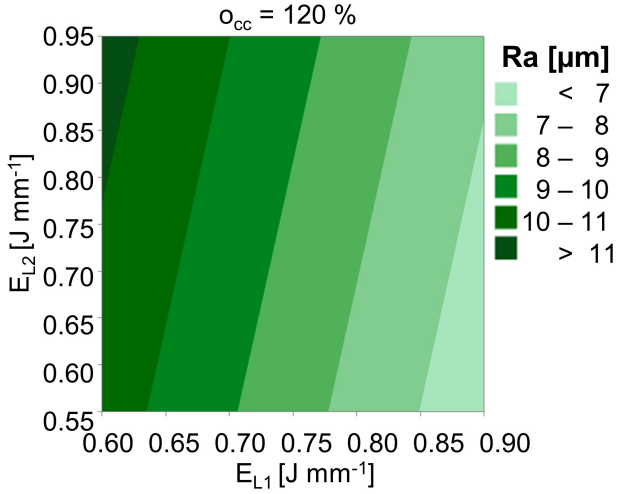

Figure 9. Contour plot in the high E_L-range of the surface roughness *Ra* vs the line energies E_{L1} and E_{L2}.

significant influence on the contour porosity, with E_{L1} having the greatest influence and the porosity increases with increasing E_{L1}, Table 7. Compared to specimens without contour parameters ($Ra = 15$ µm), high E_{L2} and low o_{cc} needs to be avoided for a decrease in surface roughness. To stay below the porosity of the infill, only contour parameters with E_L in the range of $0.6\,\mathrm{J\,mm^{-1}}$ and below and low o_{cc} can be considered.

4 Discussion

This section presents the validation of the regression models using additional parameter sets. The discussion is based on the results of the DoEs under extension of the investigation areas and supported by a qualitative assessment of the surface morphology and contour pores. On the basis of the findings, the selection of suitable contour parameters is finally carried out, which are associated with a reduction in surface roughness without increasing the porosity in the contour area.

4.1 Validation of the regression models

To validate the regression models, specimens with four additional parameter sets are built, whose roughness and contour porosity can be compared to the values predicted by the regression model. In the low E_L-range, the predicted roughness has a difference between −14.39 % and 1.60 % to the actual (measured) values, *Table 8*. A weakness of the validation specimens is that for the selected parameters the predicted values are in the range of just 1.71 µm.

In the high E_L-range the predicted roughness has a difference between −14.90 % and 16.92 % to the actual values, *Table 9*. The differences are higher compared to the model in the low E_L-range, but so is the standard deviation of the centre point. The difference between the predicted and actual porosity is significantly higher than in the roughness prediction, with up to 46.88 %. With a standard deviation of 0.05 % in the centre point and an average difference of 0.16 % (both absolute values) between the two micrographs evaluated, higher differences need to be expected. Since the porosity scatters significantly, additional characteristic values need to be included in the evaluation of the specimens. One other factor is the size of individual pores, which determines the harmfulness of the pore regarding mechanical properties [12]. The size of a pore can also provide information about its formation mechanism and thus the welding mode.

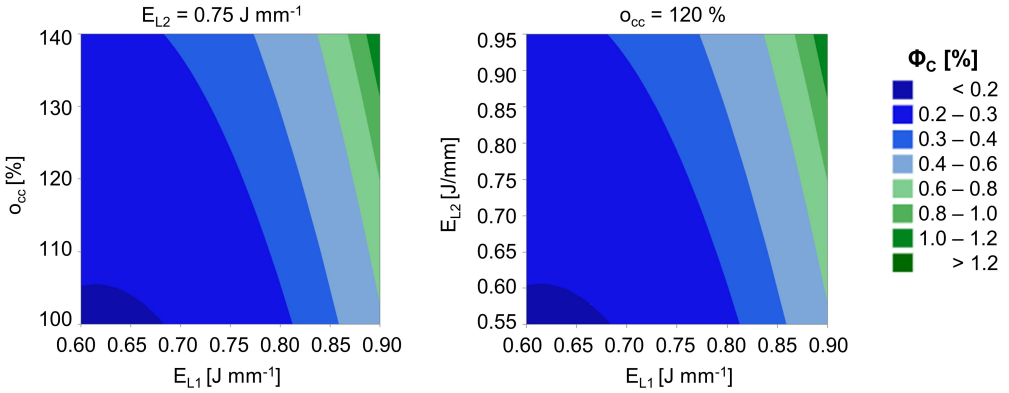

Figure 10. Contour plot in the high E_L-range of the contour porosity Φ_C vs the line energies E_{L1}, E_{L2} and the percentage overlap of the second with the first contour scan o_{cc}.

Table 8. Predicted and actual values of the surface roughness *Ra* for the validation specimens of the DoE in the low E_L-range. Standard deviation of the centre point: $\sigma = 0.53$ µm.

	o_{ci} [%]	*P* [W]	*v* [mm s^{-1}]	E_L [J mm^{-1}]	*Ra* [µm]			
					actual	pred.	Diff. (abs.)	Diff. (%)
1	60	335	850	0.39	17.79	15.23	−2.56	−14.39
2	80	335	1350	0.25	16.35	15.79	−0.56	−3.43
3	60	265	1350	0.20	14.96	15.20	0.24	1.60
4	80	265	850	0.31	16.94	16.94	0.00	0.00

Table 9. Predicted and actual values of the surface roughness *Ra* and contour porosity Φ_C for the validation specimens of the DoE in the high E_L-range. Standard deviation of the centre points: $\sigma_{Ra} = 1.22$ µm and $\sigma_{\Phi C} = 0.05$ %.

	E_{L1} [J mm^{-1}]	E_{L2} [J mm^{-1}]	o_{cc} [%]	*Ra* [µm]				Φ_C [%]			
				actual	pred.	Diff. (abs.)	Diff. (%)	actual	pred.	Diff. (abs.)	Diff. (%)
1	0.675	0.65	120	11.36	9.67	−1.69	−14.90	0.17	0.22	0.05	29.41
2	0.675	0.85	120	11.48	10.13	−1.35	−11.79	0.33	0.27	−0.06	−18.18
3	0.825	0.65	120	6.62	7.56	0.94	14.23	0.39	0.36	−0.03	−7.69
4	0.825	0.85	120	6.86	8.02	1.16	16.92	0.32	0.47	0.15	46.88

4.2 Surface roughness and morphology

The results show two E_L-ranges in which the surface roughness can be reduced by contour scans: with $E_L < 0.14$ J mm^{-1} using a pre-contour and with contour scans applying $E_L > 0.6$ J mm^{-1}. Since the lowest surface roughness is achieved with the highest investigated $E_L = 0.9$ J mm^{-1} in the first post contour, further specimens with higher E_L (one pre-contour) are investigated ($P = 370$ W, $E_L = [1.2, 1.5, 1.8, 2.4]$ J mm^{-1}). Up to $E_L = 2.4$ J mm^{-1}, no further reduction or increase in surface roughness is observed with constant values in the range of $Ra = 7 \pm 0.46$ µm. In the high E_L-range, the complete contour area is re-melted with uniform melt tracks visible on the surface, *Figure 11*D. Specimens with a low roughness of $Ra < 8$ µm reveal minimal adhesion of powder particles. Lowering E_L to 0.6 J mm^{-1} causes more powder particles to adhere to the surface, Figure 11C. The exposure of a

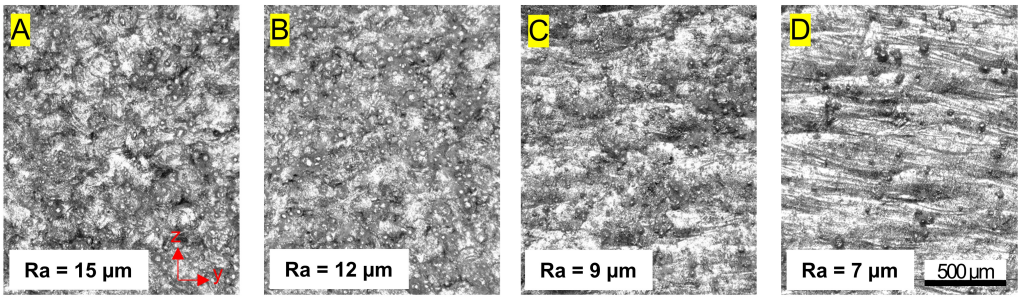

Figure 11. Surface facing the coater of specimens with different contour parameters. A) without contour parameters; B) one pre-contour: $E_L = 0.07\ \mathrm{J\,mm^{-1}}$; C) one pre-contour: $E_L = 0.6\ \mathrm{J\,mm^{-1}}$; D) two post-contours: $E_{L1} = 0.9\ \mathrm{J\,mm^{-1}}$, $E_{L2} = 0.55\ \mathrm{J\,mm^{-1}}$, $o_{cc} = 140\ \%$.

second post-contour with $o_{cc} = 100\ \%$ causes agglomerates and satellites to form on the surface, especially on the edges, *Figure 12*. These undesired features are not represented by the relatively low roughness values for *Ra* (and *Rz*), but still parameter sets with $o_{cc} = 100\ \%$ should be avoided. An explanation for the formation of those agglomerates can be the residual heat of the first post-contour, which causes local overheating when exposing the second post-contour and an uncontrolled expansion of the melt pool into the powder bed. This theory is supported by the observation that there are more agglomerates forming towards the edges of the part, where the heat conduction is reduced causing a slower cooling of the melt.

In the low E_L-range the local minimum is also at the edge of the investigated DoE. Therefore, further specimens with pre-contours down to an $E_L = 0.04\ \mathrm{J\,mm^{-1}}$ are investigated ($P = 230\ \mathrm{W}$, $E_L = [0.1,\ 0.07,\ 0.06,\ 0.05,\ 0.04]\ \mathrm{J\,mm^{-1}}$). The lowest surface roughness of $Ra = 12.3\ \mu\mathrm{m}$ is achieved at $E_L = 0.07\ \mathrm{J\,mm^{-1}}$, with the surface roughness at even lower E_L increasing towards the roughness of specimens without contour scans ($Ra = 15\ \mu\mathrm{m}$), Figure 11 B → A. Applying $E_L = 0.07\ \mathrm{J\,mm^{-1}}$ in the single track experiments leads to larger interruptions in the melt track or individual powder particles, which are only slightly fused together. Therefore, line energies in this range are initially omitted in the DoE. Nevertheless, the surface roughness can be reduced by a pre-contour in this E_L-range. This can be explained by the interaction of the contour re-melted by the melt pools of the infill. The melt pool of the infill can fill up the irregularities in the pre-contour, resulting in a more uniform surface. Surface images do not show notable differences between specimens with a pre-contour at $E_L = 0.07\ \mathrm{J\,mm^{-1}}$ and specimens without contour scans. Both show areas with powder adhesion and irregular melt pools, Figure 12A, B. Comparing cross sections in the x-y plane of the surfaces, both specimens, without contour scans and with a pre-contour at $E_L = 0.07\ \mathrm{J\,mm^{-1}}$, reveal bigger peaks and valleys than the surface at $E_L = 0.6\ \mathrm{J\,mm^{-1}}$, which is more even, *Figure 13*A, B, C.

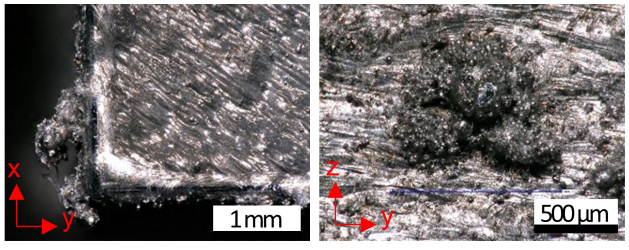

Figure 12. Surface of a specimen with an increased amount of adhering agglomerates. Parameters: two post-contours $E_{L1} = 0.9\ \mathrm{J\,mm^{-1}}$, $E_{L2} = 0.55\ \mathrm{J\,mm^{-1}}$, $o_{cc} = 100\ \%$. Left: top view, agglomerate on the edge. Right: side facing the coater, agglomerate with adhered powder particles.

4.3 Contour porosity and keyhole pores

The findings indicate a significant increase in contour porosity using contour scans with $E_L \gg 0.6\ \mathrm{J\,mm^{-1}}$ and the associated rise in the aspect ratio A_N at keyhole-mode welding. The size of the resulting pores also increases with rising line energy resulting in pores with a maximum diameter above 200 µm, *Figure 14*. In the infill area individual pores reach a maximum diameter of 100 µm and

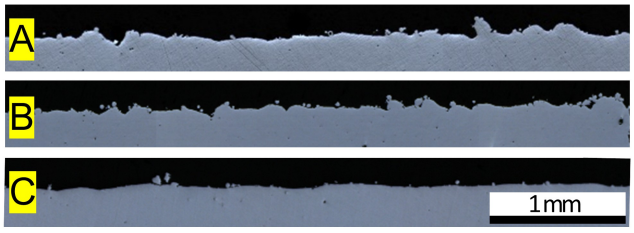

Figure 13. Cross section in the x-y plane of the surface of specimens with different contour parameters: A) without contour parameters; B) one pre-contour: $E_L = 0.07\ \mathrm{J\,mm^{-1}}$; C) one pre-contour: $E_L = 0.6\ \mathrm{J\,mm^{-1}}$.

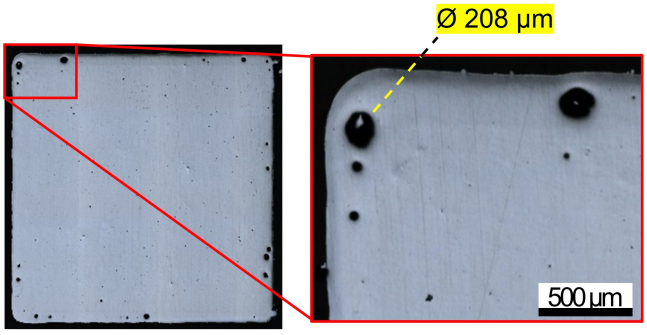

Figure 14. Cross section in the x-y plane of a specimen at a high line energy E_L with a contour porosity $\Phi_C = 0.99\ \%$ and big pores. Parameters: two post-contours, $E_{L1} = 0.9\ \mathrm{J\,mm^{-1}}$, $E_{L2} = 0.95\ \mathrm{J\,mm^{-1}}$, $o_{cc} = 100\ \%$.

thus only a quarter of the area (average largest pore diameter in the infill area considering the specimens of the DoE in the high E_L-range: 67 µm).

In the DoE at high E_L-range, attempts are made to reduce the contour porosity by re-melting the contour area when exposing a second post-contour. However, porosities that did not exceed those of the infill could only be achieved by combining the lowest E_L in both contours and $o_{cc} = 100\ \%$. By evaluating etched micrographs revealing the melt pool borders, it must be concluded, that the second contour scan does not reduce the porosity. Additional pores are rather generated, especially at a higher line energy and $o_{cc} > 100\ \%$, *Figure 15*. At $E_{L2} = 0.55\ \mathrm{J\,mm^{-1}}$ the melt pool depth of the second post-contour d_{h2} is not sufficient to re-melt the area in which keyhole pores are created in the first post-contour having a depth d_{h1}.

When using a pre-contour or two post-contours (with $E_{L2} = 0.55\ \mathrm{J\,mm^{-1}}$ and $o_{cc} = 100\ \%$) the contour porosity is in the range of the porosity of the infill at $E_L = 0.6\ \mathrm{J\,mm^{-1}}$ and below. Micrographs

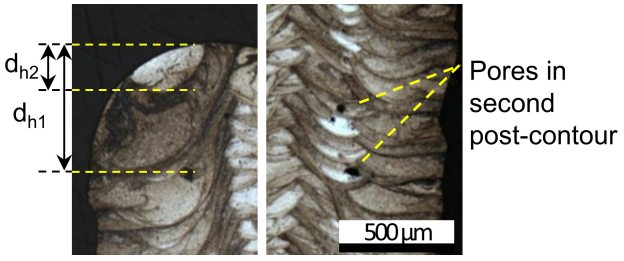

Figure 15. Etched cross section in the x-z-plane of specimens with two post-contours. Left: melt pool depth of the first (d_{h1}) and second (d_{h2}) post-contour, parameters: $E_{L1} = 0.75\ \mathrm{J\,mm^{-1}}$, $E_{L2} = 0.55\ \mathrm{J\,mm^{-1}}$, $o_{cc} = 120\ \%$. Right: pores formed due to the exposure of the second post-contour, parameters: $E_{L1} = 0.6\ \mathrm{J\,mm^{-1}}$, $E_{L2} = 0.75\ \mathrm{J\,mm^{-1}}$, $o_{cc} = 120\ \%$.

show individual pores close to the edge for both parameter sets, *Figure 16*. Since these pores are much smaller than the keyhole pores created at higher line energy, they are created more likely by evaporated gas trapped in the solidified melt. For AlSi10Mg the formation of gas pores is related to the evaporation of hydrogen, but for Scalmalloy® the evaporation of magnesium is also shown [6, 25, 26]. Due to the position of the pores at the edge of the component, they may also have formed due to the deflection of the laser beam at the end of the scan vector [27].

4.4 Selection of contour parameters

There are two E_L ranges in which the conditions of $Ra < 15$ µm and $\Phi_C < 0.2\ \%$ are met: in the range of $E_L < 0.14\ \mathrm{J\,mm^{-1}}$ when using a pre-contour with

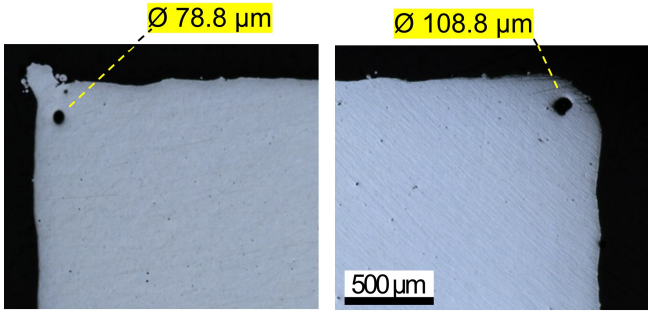

Figure 16. Cross sections in the x-y plane with singular pores in the edge of the specimens. Left: two post-contours, $E_{L1} = 0.6\ \mathrm{J\,mm^{-1}}$, $E_{L2} = 0.55\ \mathrm{J\,mm^{-1}}$, $o_{cc} = 100\ \%$. Right: one pre-contour, $E_L = 0.6\ \mathrm{J\,mm^{-1}}$.

the lowest surface roughness at $E_L = 0.07\ \mathrm{J\,mm^{-1}}$ and in the range of $E_L = 0.6\ \mathrm{J\,mm^{-1}}$ with the roughness increasing below and porosity rising above this value. Since the use of a second post-contour with $o_{cc} = 100\ \%$ creates undesired surface features, three parameter sets with $E_L = 0.6\ \mathrm{J\,mm^{-1}}$, $P = 370\ \mathrm{W}$ and $o_{ci} = 50\ \%$ are compared using a pre-contour, a post-contour and two post-contours with $o_{cc} = 120\ \%$ and $E_{L2} = 0.55\ \mathrm{J\,mm^{-1}}$. Applying two post-contours with $o_{cc} = 120\ \%$ causes pores to form in the contour area, *Figure 17*B. The specimen with a pre-contour shows a significantly lower roughness compared to specimens with a post-contour (pre-contour $Ra = 9.8\ \mu\mathrm{m}$, post-contour $Ra = 13.2\ \mu\mathrm{m}$). Therefore, at $E_L = 0.6\ \mathrm{J\,mm^{-1}}$ a pre-contour should be used.

There are different criteria based on which a selection between the two optional contour parameter sets, using a pre-contour with $E_L = 0.07\ \mathrm{J\,mm^{-1}}$ or $0.6\ \mathrm{J\,mm^{-1}}$, can be made. At the lower line energy, less edge rounding occurs and this parameter set can potentially be applied in overhang regions, where a reduced energy input is generally advantageous due to the lower heat conduction [28]. At the high line energy a lower roughness can be achieved. Additionally, roughness and contour porosity can be adjusted depending on the requirements by a slight variation of the line energy. Furthermore, the different surface morphologies of the two parameter sets need to be considered. Fewer valleys at higher line energy might lead to better mechanical performance.

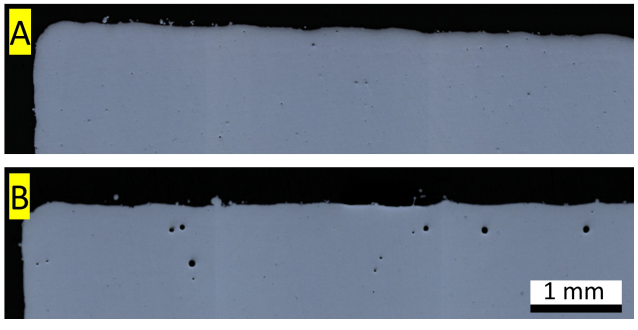

Figure 17. Cross sections in the x-y plane showing an increase in porosity when using a second post-contour with $o_{cc} = 120\ \%$. A) one pre-contour: $E_L = 0.6\ \mathrm{J\,mm^{-1}}$ B) two post contours: $E_{L1} = 0.6\ \mathrm{J\,mm^{-1}}$, $E_{L2} = 0.55\ \mathrm{J\,mm^{-1}}$, $o_{cc} = 120\ \%$.

5 Conclusion

In this study, the influence of contour parameters on the surface roughness and contour porosity of specimens made of Scalmalloy® using laser-based powder bed fusion is investigated. The aim is to reduce the roughness compared to specimens without contour parameters ($Ra = 15\ \mu\mathrm{m}$) without introducing additional pores into the contour area. After having conducted preliminary tests to determine the parameter-dependent melt pool dimensions, two parameter fields in different line energy (E_L)-ranges and with different contour scanning strategies are investigated by means of systematic design of experiments (DoE). Subsequently, the investigated parameter field is extended to further optimize the achievable part properties. The following findings are drawn:

1. A surface roughness of $Ra < 7\ \mu\mathrm{m}$ ($Rz < 55\ \mu\mathrm{m}$) is achieved using contour scans with high line energy in the range of $E_L = 0.9\ \mathrm{J\,mm^{-1}}$. A further increase of the line energy does not result in an additional reduction of the surface roughness.
2. Keyhole pores start forming in the E_L-range between $0.6\ \mathrm{J\,mm^{-1}}$ and $0.75\ \mathrm{J\,mm^{-1}}$. Applying the investigated parameters, a re-melting of the contour area could not lead to a reduction of the contour porosity.
3. The lowest roughness with parameters causing no significant increase in contour porosity is achieved using a pre-contour with $E_L = 0.6\ \mathrm{J\,mm^{-1}}$ and $o_{ci} = 50\ \%$ ($Ra = 9.8\ \mu\mathrm{m}$, $Rz = 65.2\ \mu\mathrm{m}$).
4. A reduction in roughness at low line energies can only be achieved by utilizing a pre-contour scan. The lowest roughness $Ra = 12.3\ \mu\mathrm{m}$ ($Rz = 78.4\ \mu\mathrm{m}$) is achieved at $E_L = 0.07\ \mathrm{J\,mm^{-1}}$ and $o_{ci} = 50\ \%$.
5. There are use cases for both contour parameter sets, although the influence on the mechanical properties needs further investigation.

Acknowledgements

The authors thank the German Federal Ministry of Education and Research (BMBF) for funding the joint project “Operational strength of additively manufactured components - BadgeB” (funding number: 02P15B154) within the framework of the

ProMat 3D funding measure managed by the Project Management Agency Karlsruhe (PTKA). The support made the described investigations and presented results possible. Open access funding enabled and organized by Projekt DEAL.

6 References

[1] A. Gebhardt, *Additive Fertigungsverfahren*, Hanser Verlag, München, **2016**.
[2] M. Awd, J. Tenkamp, M. Hirtler, S. Siddique, M. Bambach, F. Walther, *Materials* **2017**, *11*, 17.
[3] P. Rometsch, Q. Jia, K.V. Yang, X. Wu, *Add. Man. f. t. Aerosp. Ind.* **2019**, 301.
[4] K. Schmidtke, F. Palm, A. Hawkins, C. Emmelmann, *Phsics Procedia* **2011**, *12*, 369.
[5] A.B. Spierings, *Ph.D. Thesis*, ETH Zürich, Switzerland, **2018**.
[6] K. Schmidtke, *Ph.D. Thesis*, TU Hamburg, Germany, **2019**.
[7] Y. Shi, P. Rometsch, K. Yang, F. Palm, X. Wu, *Materials Letters* **2017**, *196*, 347.
[8] D. Koutny, D. Skulina, L. Pantelejev, B. Lenczowski, F. Palm, A. Nick, *Procedia CIRP* **2018**, *74*, 44.
[9] J. Fischer, *Ph.D. Thesis*, TU Darmstadt, Germany, **2019**.
[10] M. Rasch, F. Huber, L. Butzhammer, C. Merz, M. Schmidt, presented at *14th Rapid.Tech Conference*, Erfurt, Germany, June 20 – June 22, **2017**, pp. 256–268.
[11] Z. Chen, S. Cao, X. Wu, C.H.J. Davis, *Add. Man. f. t. Aerosp. Ind.* **2019**, 283.
[12] A. du Plessis, I. Yadroitsava, I. Yadroitsev, *Mat. and Des.* **2020**, *187*.
[13] W.E. King, H.D. Barth, V.M. Castillo, G.F. Gallegos, J.W. Gibbs, D.E. Hahn, C. Kamath, A.M. Rubenchik, *Journ. o. Mat. Proc. Techn.* **2014**, *12*, 2915.
[14] M. Bayat, A. Thanki, S. Mohanty, A. Witvrouw, S. Yang, J. Thorborg, N.S. Tiedje, J.H. Hattel, *Additive Manufacturing* **2019**, *30*, 18.
[15] A.J. Birnesser, *Prozessregelung beim Laserstrahlschweißen*, Herbert Utz Verlag, München, Germany, **2011**.
[16] C. Tenbrock, F.G. Fischer, K. Wissenbach, J.H. Schleifbaum, P. Wagenblast, W. Meiners, J. Wagner, *Journ. o. Mat. Proc. Tech.* **2020**, *278*.
[17] J. Trapp, A.M. Rubenchik, G. Guss, M.J. Matthews, *App. Mat. Tod.* **2017**, *9*, 341.
[18] J.-P. Kruth, M. Badrossamay, E. Yasa, J. Deckers, J. van Humbeeck, presented at *16th Int. Symp. o. Electrom.*, Shanghai, China, April 19, **2010**.
[19] E. Yasa, *Ph.D. Thesis*, KU Leuven, Belgium, **2011**.
[20] R. Rashid, S.H. Masood, D. Ruan, S. Palanisamy, R.A. Rahman Rashid, M. Brandt, *Journ. o. Mat. Proc. Techn.* **2017**, *249*, 502.
[21] S. Kleszcynski, presented at *26th Int. SSF Symp.*, Austin, USA, August 10 – August 12, **2015**, 360.
[22] S. Edelhäuser, L. Hümmeler, P. Hofbauer, C. Schmitt, World Patent 197443A1, **2018**.
[23] N.T. Aboulkhair, N.M. Everitt, I. Ashcroft, C. Tuck, *Additive Manufacturing* **2019**, *1*, 77.
[24] *DIN EN ISO 4288*, Beuth Verlag, Berlin, Germany, **1998**.
[25] C. Weingarten, D. Buchbinder, N. Pirch, W. Meiners, K. Wissenbach, R. Poprawe, *Journ. o. Mat. Proc. Tech.* **2015**, *221*, 112.
[26] R. Li, M. Wang, T. Yuan, B. Song, C. Chen, K. Zhou, P. Cao, *Powder Technology* **2017**, *319*, 117.
[27] A.A. Martin, N.P. Calta, S.A. Khairallah, J. Wang, P.J. Depond, A.Y. Fong, V. Thampy, G.M. Guss, A.M. Kiss, K.H. Stone, C.J. Tassone, J. Nelson Weker, M.F. Toney, T. van Buuren, M.J. Matthews, *Nature communications* **2019**, *10*, 1987.
[28] H. Chen, D. Gu, J. Xiong, M. Xia, *Journ. o. Mat. Proc. Tech.* **2017**, *250*, 99.

Received in final form: November 20th 2020

